Towards time-resolved measurement of valley polarisation by second harmonic generation

Marken Foo Yong Wen

Supervisor:

Assistant Professor José Carlos Viana-Gomes

Co-supervisor:

Associate Professor Goki Eda

A thesis submitted for the degree of Bachelor of Science with Honours

Department of Physics

National University of Singapore

2019

Acknowledgements

Abstract

In this thesis, we describe and discuss the implementation of an experiment to measure valley polarisation in a transition metal dichalcogenide (TMD) sample using second harmonic generation (SHG). A pump-probe setup is used, pumping valley polarisation in the TMD with circularly-polarised light and probing with linearly-polarised light. The change in polarisation of the generated second harmonic is to be measured to determine the degree of valley polarisation present in the sample.

A discussion is given on various issues on the way to constructing a working setup. It is noted that preserving the signal polarisation is a key factor in a successful implementation. By using SHG and sum frequency generation as diagnostics, we verify that the constructed setup is well-aligned and ready for data collection.

Table of contents

Chapter 1: **Introduction**

The study of 2D materials has led to many new developments and opens doors to new technological applications. One notable domain in this field is valleytronics, the study of the valley degree of freedom. The valley degree of freedom is a pseudospin property possessed by charge carriers in certain 2D materials. It may be coupled to, but is distinct from the electronic spin, and constitutes a new degree of freedom which can be manipulated. This enables potential new designs in nanoscale engineering and optoelectronics exploiting this degree of freedom, and there may even be potential to use this degree of freedom to construct qubits [1].

A valley polarisation – an imbalance in the number of charge carriers with the "+" or "-" valley property – can be induced in a sample, and a key step in the manipulation of valleys is to be able to detect such an imbalance. As the valleys each couple strongly with different-handed circularly polarised light, a valley polarisation can be induced by optical means, and it is therefore natural to seek an optical means to detect the same.

Time-resolved valley polarisation measurements have already been achieved with the phenomena of photoluminescence and Kerr rotation. However, both have constraints on the materials they can be used on; the former requires a direct bandgap, the latter requires strong spin-orbit coupling. An alternative means of detecting valley polarisation has been proposed, involving measuring the polarisation of second harmonic generation (SHG) [2]. An experimental proof-of-concept been accomplished by my supervisor's group [3] only recently, which shows promise that the technique can be further developed.

In this thesis, I will describe how SHG can be used to investigate the valley polarisation of a material, and our efforts to build a pump-probe setup to achieve this.

This thesis is organised as follows: Chapter 2 presents the relevant theory behind the experiment, namely explaining what valley polarisation is, nonlinear optics and how the two can be related. Chapter 3 describes the original experimental setup and discusses the issue we had in preserving the polarisation of the SHG signal. Chapter 4 presents the modifications made to the setup to address the issue, and discusses diagnostic tests using SHG and sum frequency generation to check that the setup is well-aligned and functional.

Chapter 2: **Theory**

2.1 Valleys in 2D materials

Valley polarisation involves the "valley" degree of freedom of charge carriers in a crystal. The interest in this degree of freedom is that it provides an additional property of the charge carriers that can potentially be controlled. There are potential applications in quantum computing (using the valley degree of freedom as a qubit), nanoscale engineering and optoelectronics.

The valley property is well-studied in certain classes of 2D materials, including graphene [4], [5] and TMDs (transition metal dichalcogenides) [6], [7]. The advantage of the latter is that TMD monolayers intrinsically have no inversion symmetry, unlike graphene, and the lack of inversion symmetry is a necessary condition for the two types of valleys to be distinguished. Notable examples include tungsten diselenide (WSe_2) and molybdenum disulfide (MoS_2).

2.1.1 Transition metal dichalcogenides and valleys

TMDs have the chemical formula MX_2, where M is a transition metal (e.g. Mo, W) and X is an element from Group VI of the periodic table (e.g. S, Se, Te). These can be arranged in a monolayer, with a 3-atom basis and a triangular lattice structure, resulting in a 2D material. Viewed from the top, the crystal has a "honeycomb" structure like graphene (Figure 1). It has D3h point group symmetry (roughly speaking, a threefold rotation axis), which influences some of its properties like its optical nonlinear susceptibility and the presence of valleys.
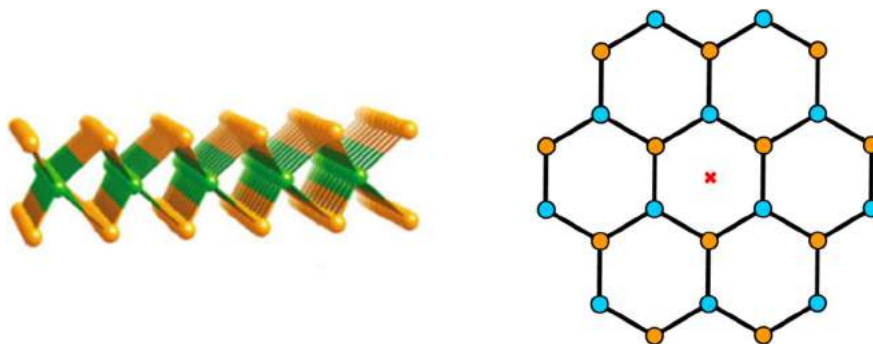

Figure 1 - Structure of a TMD. Left: Side view of a TMD monolayer. Orange atoms are chalcogen, green atoms are transition metal. Source: Kolobov, A. V., & Tominaga, J. (2016). Right: Top view of a TMD, with the D3h symmetry axis marked with a red cross.

Due to the D3h point group symmetry of the crystal lattice, its first Brillouin zone (FBZ) is hexagonal and has the corresponding D3h symmetry in k-space. At the vertices of the FBZ, the electronic band structure of monolayer or few-layer TMDs have local minima in the conduction band and local maxima of the valence band. These are referred to as the valleys of the TMD.

Owing to the D3h symmetry of the FBZ in TMDs, the six valleys can be distinguished into two sets of three, labelled +K and -K. Charge carriers in these two types of valleys can be grouped via certain couplings with other physical phenomena, for instance left- and right-handed circularly polarised light [8].
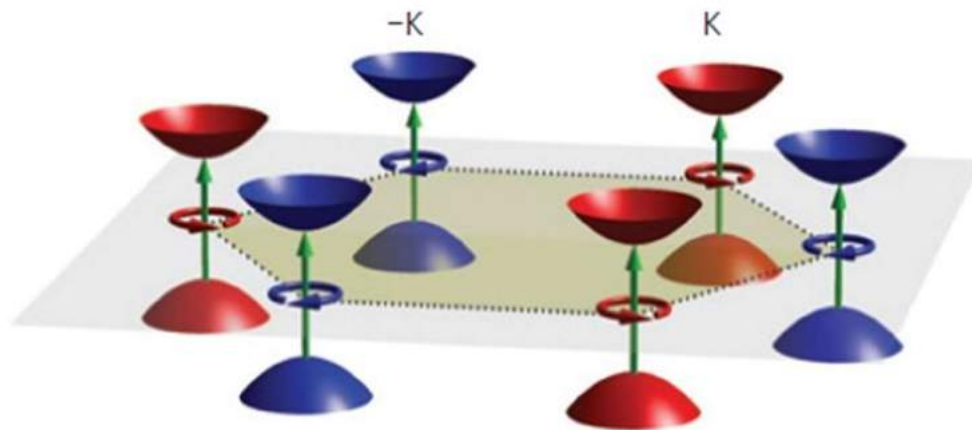
Figure 2 - The +K (red) and -K (blue) valleys of the FBZ of a TMD. Also pictured are σ+ and σ- photons (in green) coupling to the +K and -K valleys respectively, exciting charge carriers in the corresponding valley. Source: Xu, X., Yao, W., Xiao, D., & Heinz, T. F. (2014).

2.1.2 Origin of valleys from topology of energy bands

The discussion in this section stems from sources such as [9], [10].

In quantum mechanics, the Berry phase is a phase accumulated during an adiabatic evolution of a quantum state along a closed path in its native space. Depending on the topology of the space and the closed path taken, when the state returns to its original state, it will have picked up an additional phase known as the Berry phase.

This can be seen as follows. When the evolution of the system is described by some varying set of parameters λ, the overall phase picked up can be written as $\phi = \oint \langle u_\lambda | i \nabla u_\lambda \rangle \cdot d\lambda$, where the state $|u_\lambda\rangle$ is the state the system is in for a given set of

parameters λ. This phase ϕ is the Berry phase. It will only depend on the topology of the space and the closed path chosen.

The term within the integral $\mathbf{A}_\lambda = \langle u_\lambda | i\boldsymbol{\nabla} u_\lambda \rangle$ is referred to as the Berry connection (emphasising its mathematical nature) or the Berry potential (emphasising its physical consequences). In a three-dimensional parameter space (like k-space), the line integral can be reinterpreted as a surface integral by Stokes' theorem:

$$\oint \langle u_\lambda | i\boldsymbol{\nabla} u_\lambda \rangle \cdot d\boldsymbol{\lambda} = \int (\boldsymbol{\nabla} \times \langle u_\lambda | i\boldsymbol{\nabla} u_\lambda \rangle) \cdot d\mathbf{S} = \int \boldsymbol{\Omega}(\lambda) \cdot d\mathbf{S}$$

Where the line integral on the left is over some closed path and the integral on the right is over the area enclosed by the path. The quantity $\boldsymbol{\Omega} = \boldsymbol{\nabla} \times \mathbf{A}$ is the Berry curvature, a quantity expressing how "curved" the parameter space is in a topological sense. It can also be interpreted as a sort of magnetic field in the parameter space, arising from the curl of the Berry potential. This Berry curvature is gauge-invariant, gauge being the choice of how the accumulated Berry phase is distributed along the path parametrised by λ.

In the k-space of a TMD (D3h symmetry), the parameter in question is the quasi-momentum $\mathbf{k}$, so $\lambda = \mathbf{k}$. We can then calculate the Berry curvature in the energy bands using the definition of the Berry potential above, where the states $|u_\mathbf{k}\rangle$ are taken to be the periodic part of the energy eigenfunctions. (If we were to include the aperiodic part of the Bloch functions as $e^{i\mathbf{k}\cdot\mathbf{r}}|u_\mathbf{k}\rangle$, it would average to zero.)

Explicitly calculating this, we have $\boldsymbol{\Omega}(\mathbf{k}) = \boldsymbol{\nabla} \times \mathbf{A}(\mathbf{k}) = i\langle \boldsymbol{\nabla}_\mathbf{k} u_\mathbf{k} | \times | \boldsymbol{\nabla}_\mathbf{k} u_\mathbf{k}\rangle$.

Now we consider what happens under inversion and time-reversal symmetries. Under inversion symmetry, the direction of $\mathbf{k}$ and the derivatives change signs, so $\boldsymbol{\Omega}(\mathbf{k}) = \boldsymbol{\Omega}(-\mathbf{k})$; thus, if there is inversion symmetry in k-space, the two valleys +K and -K at opposite ends of the FBZ will have identical Berry curvatures and thus be indistinguishable (as in graphene for instance, barring some other means of breaking the inversion symmetry).

Under time-reversal symmetry, the cross product will also pick up a minus sign, and hence $\boldsymbol{\Omega}(\mathbf{k}) = -\boldsymbol{\Omega}(-\mathbf{k})$. In general, we thus have the important result that the Berry curvatures in opposite valleys will be of opposite sign.

The symmetry and gauge invariance properties of the Berry curvature strongly suggest it can manifest itself via physical phenomena. Charge carriers (electrons, holes excitons) in opposite valleys will see opposite Berry curvatures and thus have contrasting "valley" properties. Well-known examples of phenomena emerging from this are discussed in [10].

2.1.3 Inducing and measuring valley polarisation

A TMD in its ground state will have an equal number of charge carriers in the +K and -K valleys. However, when there is an imbalance in the valley populations, the material acquires an overall valley polarisation which can be used to encode information.

The valley polarisation can be measured in several ways, including the presence of an anomalous "valley current" due to the valley Hall effect [11], or a Kerr rotation of the polarisation of incident polarised light due to the Valley Stark effect [12], [13].

Conversely, a valley polarisation can be brought about by selective excitations of electrons in a particular valley. This can be done optically using circularly polarised light, which couples selectively with one of the valleys [14]. This is in part because circular polarisation, like the Berry curvature, shares the same symmetry under time-reversal. Weak spin-orbit coupling also breaks the degeneracy of the spin-up and spin-down levels in the conduction band in different ways for each valley, resulting in different optical selection rules for each valley.

In the course of my Honours project, I worked on an experimental setup aiming to probe the valley polarisation with a novel method, by measuring the polarisation state of light produced by the crystal's second harmonic generation (SHG). The valley polarisation changes the second-order nonlinear susceptibility tensor properties of the crystal, thus changing the polarisation state of the generated SHG. This change can be measured and thus gives information about the valley polarisation. This has been theoretically calculated to work in graphene [2], [15], but only recently experimentally observed [3].

2.2 Nonlinear optical processes and valleys

Nonlinear optical processes refer to processes which depend nonlinearly on the incident optical electric fields. In general, we can relate the electric polarisation of the optical medium **P** with the electric field in the medium **E** via the following tensorial relation (terms up to second order included):

$$P_i = \epsilon_0 \chi_{ij}^{(1)} E_j + \epsilon_0 \chi_{ikl}^{(2)} E_k E_l + \cdots,$$

where we have used the Einstein summation convention. ϵ_0 is the vacuum permittivity, $\chi_{ij}^{(1)}$ is the linear susceptibility and $\chi_{ikl}^{(2)}$ is the second-order nonlinear susceptibility of the material for the process in question. The electric component of an applied optical field will contribute to **E** and therefore to **P**.

2.2.1 Second harmonic generation (SHG)

Second harmonic generation (SHG) is a nonlinear optical process whereby two photons of the same frequency combine to yield a single new photon with twice the frequency of the input photons. The radiated optical field is directly proportional to the nonlinear component of the electric polarisation of the material, i.e.

$$E_i^{(out)}(\omega) \propto P_i^{(2)}(\omega) = \epsilon_0 \chi_{ijk}^{(2)}(\omega; \omega_1, \omega_2) E_j(\omega_1) E_k(\omega_2)$$

where the brackets indicate the frequency associated with each quantity. In the case of SHG, $\omega = \omega_1 + \omega_2$ and $\omega_1 = \omega_2$. (If $\omega_1 \neq \omega_2$, then we have the case of sum-frequency generation or SFG instead.)

As a second-order nonlinear process, it can only occur in materials without inversion symmetry [16], which as in the case of TMDs.

The application of SHG to probe valley polarisation lies in the fact that the polarisation of the output frequency-doubled photons depends not only on the polarisation of the input photons, but also the symmetry group and orientation of the nonlinear medium.

A calculation demonstrates this dependence. We consider the specific case of a nonlinear medium of symmetry group D3h. The general tensorial relation for the second-order nonlinear polarisation **P** in matrix form is:

$$\begin{pmatrix} P_x \\ P_y \\ P_z \end{pmatrix} = \begin{pmatrix} d_{11} & d_{12} & d_{13} & d_{14} & d_{15} & d_{16} \\ d_{21} & d_{22} & d_{23} & d_{24} & d_{25} & d_{26} \\ d_{31} & d_{32} & d_{33} & d_{34} & d_{35} & d_{36} \end{pmatrix} \begin{pmatrix} E_x^2 \\ E_y^2 \\ E_z^2 \\ 2E_yE_z \\ 2E_zE_x \\ 2E_xE_y \end{pmatrix}$$

In this form, we have simplified the 27-element χ tensor into the 18-element $\mathbf{d}$ tensor by asserting that the order of the incident electric fields does not matter, i.e. $E_xE_y = E_yE_x$ and so on.

We will further assume that the incident optical beam(s) is (are) normal to the crystal's surface, such that the associated electric and magnetic fields are in the plane of the crystal. This eliminates the z-coordinate from consideration. The relation simplifies to:

$$\begin{pmatrix} P_x \\ P_y \end{pmatrix} = \begin{pmatrix} d_{11} & d_{12} & d_{16} \\ d_{21} & d_{22} & d_{26} \end{pmatrix} \begin{pmatrix} E_x^2 \\ E_y^2 \\ 2E_xE_y \end{pmatrix}$$

Furthermore, if the crystal has D3h symmetry, the $\mathbf{d}$ tensor simplifies to depend on one independent parameter [16]. Choosing the x and y coordinates to correspond to the zigzag and armchair directions of the crystal respectively, we have

$$\begin{pmatrix} P_{zz} \\ P_{ac} \end{pmatrix} \propto \begin{pmatrix} 0 & 0 & -\chi_{int} \\ -\chi_{int} & \chi_{int} & 0 \end{pmatrix} \begin{pmatrix} E_{zz}^2 \\ E_{ac}^2 \\ 2E_{zz}E_{ac} \end{pmatrix}$$

As such the output optical beam of doubled frequency will have a polarisation that depends both on the input beam's polarisation, as well as the relative orientation of the crystal to the polarisation axes. This is the intrinsic SHG of the crystal, due purely to the crystal structure.

2.2.2 SHG and valley polarisation

A TMD monolayer has D3h symmetry, and so will exhibit the SHG behaviour above. Its FBZ in k-space has the same D3h symmetry. In the ground state the charge carrier populations in the two types of valleys will be the same, so their contributions cancel out overall, but if there is a net population imbalance between the two valleys, the valley polarisation will also contribute to the nonlinear susceptibility [2]:

$$\begin{pmatrix} P_{zz} \\ P_{ac} \end{pmatrix} \propto \begin{pmatrix} \chi_{vp} & -\chi_{vp} & -\chi_{int} \\ -\chi_{int} & \chi_{int} & -\chi_{vp} \end{pmatrix} \begin{pmatrix} E_{zz}^2 \\ E_{ac}^2 \\ 2E_{zz}E_{ac} \end{pmatrix}$$

The valley polarisation adds new nonlinear susceptibility components. This is due to the D3h symmetry in k-space being rotated 90° with respect to real space, so it does not add to the same susceptibility tensor components as the intrinsic contribution does.

2.2.3 Principle of measuring SHG polarisation

The above calculations suggest a method to measure valley polarisation in a TMD. First, a TMD sample is prepared, and a probe laser of sufficiently high intensity impinges upon it (at normal incidence, to keep the calculations above simple). If the probe laser is at a frequency off-resonant from the valley bandgap and not circularly polarised, the TMD sample does not acquire a valley polarisation, and the intrinsic SHG response can be measured from the produced second harmonic beam (either transmitted or reflected from the sample).

Next, if a circularly-polarised pump laser excites the TMD sample near the valley bandgap frequency, a valley polarisation will be induced, and this will cause a change in the SHG signal's polarisation. The amount of valley polarisation will be linked to the strength of its contribution to the nonlinear susceptibility of the TMD and thus to the shift in SHG polarisation. This provides a means in principle to quantitatively measure the valley polarisation via second harmonic generation.

In order to measure the polarisation of a laser, the one possible method is to pass it through a linear polariser whose orientation can be controlled (referred to as an analyser), then measuring the transmitted intensity of the beam. By plotting the transmitted intensity against the analyser's angle, we can get a visual representation of the laser's polarisation. Such a representation is shown in Figure 3, and the corresponding setup in Figure 4.
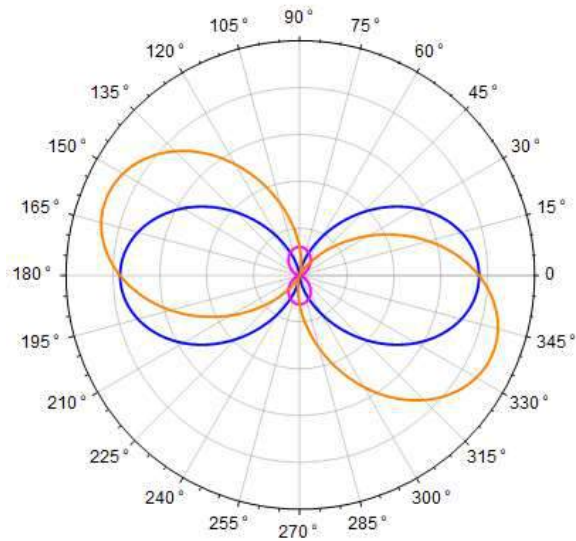

Figure 3 - Mathematica calculation of second-harmonic signal generated from linearly-polarised light normally incident on a TMD. The polarisation axis is parallel to the zigzag direction of the lattice. The plots are of intensity against analyser angle. Blue: Intrinsic SHG contribution from real lattice. Purple: SHG contribution from valley polarisation. Orange: Resultant SHG. χ_{vp} is assumed to be $0.4\chi_{int}$.
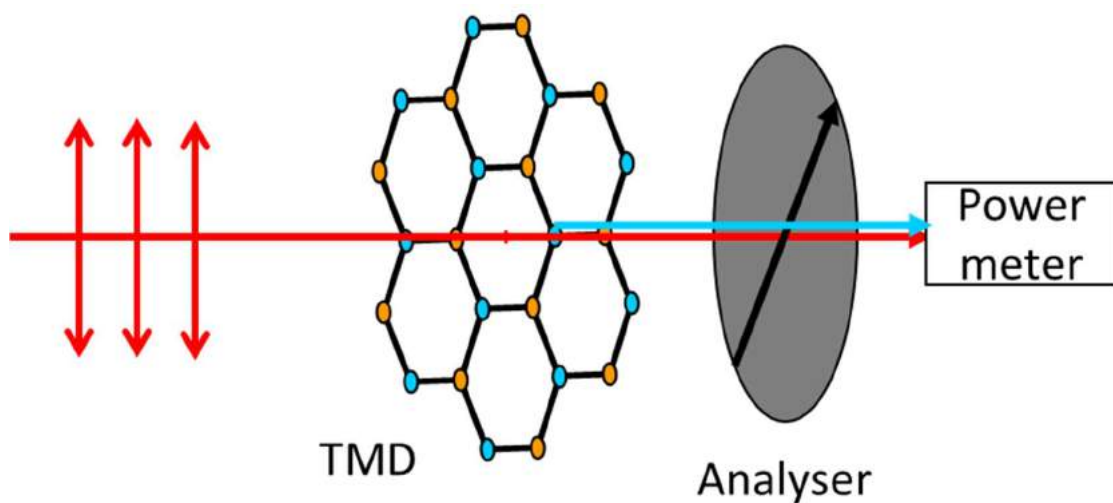

Figure 4 – A hypothetical setup to obtain the graph shown in Figure 3. The incident light beam is initially polarised in the zigzag direction of the TMD. A second harmonic beam is generated, sent through a polariser, then its intensity is measured.

From Figure 3, we can note several details. The blue curve is the intrinsic SHG contribution, the purple from the valley polarisation contribution, and the orange is the net SHG signal seen. The contribution due to valley polarisation is indeed at 90° to the intrinsic contribution, and the overall SHG signal thus has a larger maximum and is rotated a small amount compared to the intrinsic linearly-polarised signal. This rotation of linear incident polarisation is what can be measure experimentally; the amount of rotation can give quantitative information about the degree of valley polarisation present in the sample.

Chapter 3: **Experiment**

As described in section 2.2.3, a possible basic setup to measure valley polarisation via second harmonic generation involves:

- A pump beam to excite valley polarisation
- A probe beam to get an SHG signal
- A means to analyse the polarisation of the signal

An experimental proof-of-concept had been recently achieved by my group, one-beam SHG of WSe_2 [3]. Now to achieve better control over the valley polarisation and enable time-sensitive measurements using SHG, constructing a working pump-probe setup is the goal.

In this chapter, I will briefly discuss the motivation behind this experiment, followed by the evolution of the setup and my role in it.

3.1 Motivation for the experiment

The prior experimental proof-of-concept had used a single-beam setup, using the same beam to pump a valley imbalance and generate a second harmonic signal. By now separating the pump and probe beam, it is possible to achieve time-resolved measurements of valley polarisation using pulsed lasers. This can yield information such as the initialisation time and lifetime of valley polarisation in the material. If successful, this would put SHG as a viable time-resolved method of measuring valley polarisation alongside photoluminescence (PL) [17] and Kerr rotation measurements [13].

SHG would offer some advantage over the other methods in that there are fewer constraints on the physical properties of the sample being measured; all that is required is that the two distinct types of valley are present, and that the material exhibit a second-order nonlinear optical behaviour.

PL spectroscopy requires bright excitonic states; in other words, the sample in question needs to have a direct bandgap at the K points. There is no such requirement for SHG.

Kerr rotation on the other hand requires the sample to have strong spin-orbit coupling. The phenomenon of regular Kerr rotation depends on the existence of an out-of-plane magnetic field in the sample. In valley-induced Kerr rotation, we require the spin-orbit coupling to significantly break the degeneracy of the conduction band energies in the valleys, such that spin-up is the lower conduction level in the +K valley and spin-down in the -K valley. When a valley imbalance is created, it is coupled to the spin, resulting in a net spin moment at the surface of the sample. The degree of Kerr rotation would thus be linked to the valley polarisation via spin-orbit coupling [6]. Once again, there is no such requirement for SHG.

3.2 Basic design of experiment

When I joined the group working on this experiment, the setup was still in the process of being built and evolved. My role in the course of this Honours project was therefore mostly in building and aligning the setup, troubleshooting and changing it to accommodate problems that might have appeared, as well as coding some calculations and data acquisition routines for the setup.

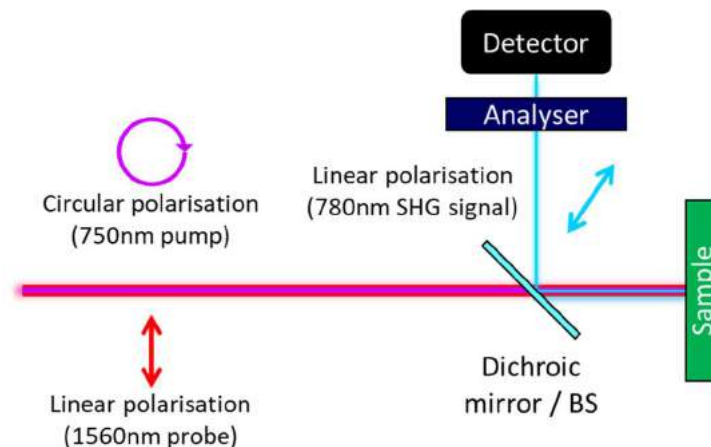The basic schematic underlying all versions of the setup is as follows.

Figure 5 - Schematic of the basic principle behind the experiment.

The circularly-polarised pump tuned to around 750nm and linearly-polarised 1560nm probe beams are collimated and sent to the sample. When pulses from each arrive at the sample at the same time, rotation of the SHG occurs (compared to when only the

1560nm beam arrives) and the second harmonic signal reflected from the substrate is extracted. Its polarisation is analysed by means of an analyser (rotating polariser) and a sufficiently sensitive detector behind (a spectroscope, a photomultiplier tube, an avalanche photodiode, etc.)

In order to acquire the desired signal, the pump and probe pulses must arrive at the same spot on the sample within a short time of each other. To maximise the signal, the beam waists must therefore be overlapped in space (transverse and longitudinal directions), and the pulses must be overlapped in time. This introduces some design choices.

- The pulsed beams should be synchronous to achieve better temporal pulse overlap.
- A delay line should be introduced to control the arrival time of the pulses.
- The transverse position of the beams can be controlled by aligning mirrors and other optical components.
- A separate telescope (lens) for at least one beam should be included to control the relative longitudinal position of the beam waists at the sample.
- The beams should be collimated and combined using dichroic mirrors or beam splitters.
- The SHG signal should be extracted from the pump beams by similar means before being analysed.

The reflected second harmonic signal is measured instead of the transmitted signal for practical reasons. Firstly, it does not limit the choice of substrate, which would have to be transparent in the desired optical range if we had chosen to measure the transmitted signal instead. Secondly, foreseeing the value of using a cryostat to cool the sample and reduce thermal effects, using the reflected signal is more appropriate here.

3.3 Samples

The samples we had used to calibrate and attempt to see intermediate results with while building the setup are:

- As the actual sample we wish to measure, monolayer tungsten diselenide (WSe_2), a TMD. As a monolayer, its response will be weak, hence the need for two other samples for testing and debugging of the setup.

- For debugging purposes: Bulk lithium niobate (LiNbO$_3$, "LNB"), which has a strong second-order susceptibility and so is useful to test for alignment of the setup.

- For debugging purposes: 3R-phase molybdenum disulfide (MoS$_2$), a TMD. In the 3R phase, even layer-stacks do not exhibit inversion symmetry unlike the 2H phase, so there is still a sizable second-order optical susceptibility.

The samples were not prepared by me, but by the group of A/Prof. Eda. The TMDs were transferred onto silicon substrates and encapsulated with hexagonal boron nitride (HBN). Neither the substrate nor the HBN give nonlinear optical responses [18], so they will not affect the experiment.

3.4 Initial experimental setup

When I first joined the group, the relevant part of the experimental setup had been as follows:
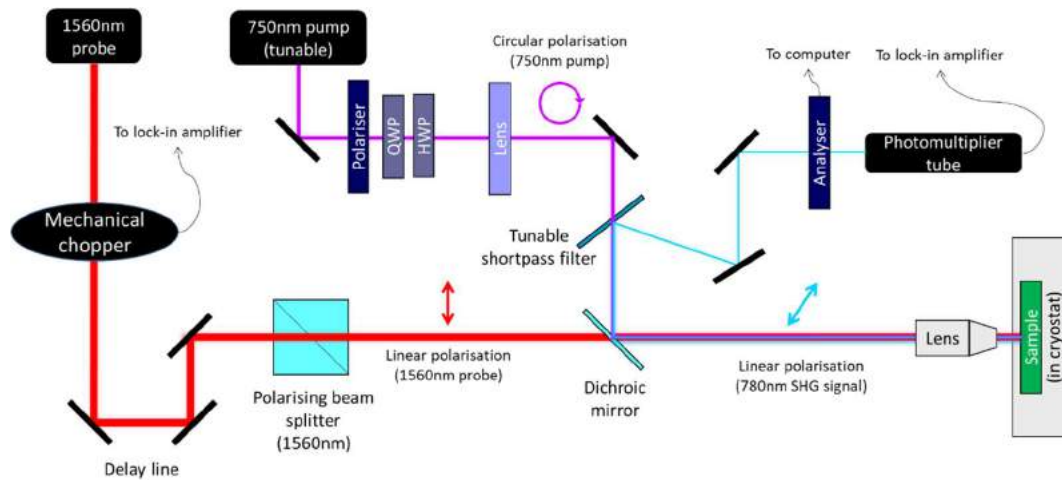

Figure 6 - Initial experimental setup.

The probe beam is the 1560nm output from a FemtoFiber pro NIR from Toptica Photonics. It is an 80MHz pulsed laser, output 1560nm with FWHM of about 20nm. This wavelength is off-resonance from the bandgap of most TMDs (which are mostly in the visible range), so will be appropriate as a probe beam without significantly affecting the valley polarisation itself. We choose it to be linearly polarised, which yields a linearly-polarised but rotated second harmonic signal in the presence of valley

14

polarisation in the sample. The rotation of the polarisation angle is what we wish to measure.

The pump beam is a home-built tunable pulsed supercontinuum (SC) laser built from the same FemtoFiber pro NIR laser output. It is thus also at 80 MHz, and the wavelength is tuned to around 750nm for the experiments. This is close to the bandgap of WSe2 (1.7eV [19]) and MoS2 (1.8eV [20]), so can be used to pump valley polarisation when circularly polarised. The tunability allows it to be tuned to the bandgap of various materials we may wish to study, enhancing the flexibility of the setup. Its power is considerably lower than the probe beam (used to generate SHG) to avoid saturating the valley polarisation.

As discussed in section 3.2, the probe beam is linearly polarised and goes through a home-built delay line, while the pump beam is circularly polarised and passes through a lens to control the longitudinal position of its beam waist near the sample. These components allow the beams' overlap in both time and space to be controlled.

The delay line can shift up to 12mm with resolution of up to 0.001mm to align the pulses.

A dichroic mirror is used to combine the 1560nm probe and 750nm pump beams, while a 100x lens is used to focus them onto the sample to achieve the high irradiance necessary for SHG.

The reflected SHG signal is then reflected by the dichroic mirror and separated from the SC pump beam by a properly-angled tunable shortpass filter (VersaChrome Edge 790nm tunable shortpass filter from Semrock). It is then sent through an analyser and measured with a photomultiplier tube connected to a lock-in amplifier. The analyser is mounted on a motorised rotation stage and controlled via a computer using Python code. The reference frequency sent to the lock-in amplifier is from a mechanical chopper on the probe beam.

3.5 Troubleshooting issue – unexpected polarisation change

When testing the setup, it was clear that something was not behaving correctly. Using only the linearly polarised probe beam, the expected linear second harmonic signal

would come out rotated, or even elliptical. By placing the analyser at various locations and isolating various subsystems, it was determined that the combination of the dichroic mirror, the tunable filter, and the dielectric mirrors after the tunable filter were modifying the polarisation.

To confirm where the issue was, I built a small setup to check the polarisation of the reflected and transmitted beams of each optical component, given some incident polarised beam.
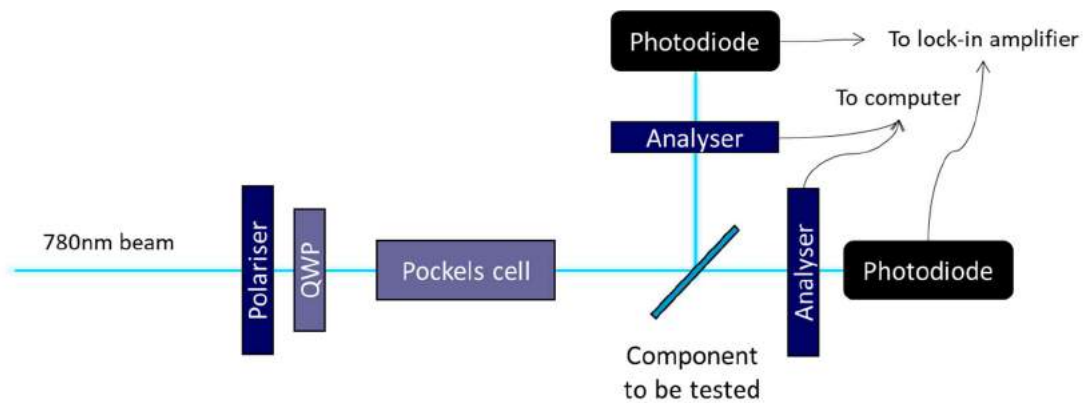
3.5.1 Polarisation testing setup

Figure 7 - Setup to test polarisation behaviour of components.

The 780nm output from the Toptica FemtoFiber pro NIR laser was used. The input polarisation to the component was controlled via a fixed linear polariser, a quarter-wave retarder (QWP) and a Pockels cell (a variable retarder controlled by applying an external voltage across it). For linear polarisation, the QWP and Pockels cell would be absent or aligned such that their fast axes were aligned to the polarisation axis. For circular or elliptical polarisation, the QWP and Pockels cell were aligned such that their fast axes were at 45° to the polarisation axis, and the voltage supplied to the Pockels cell tuned to provide the appropriate output polarisation.

The component to be tested would be placed after the Pockels cell, and the reflected and/or transmitted beams would each be analysed by passing it through a polariser mounted in a computer-controlled rotational stage, then measured with a photodiode connected to a lock-in amplifier.

To take data, I wrote some code to automate the analyser rotation and photodiode measurement taking in Python.

16

3.5.2 Calibration

Calibration of the setup was done in order to characterise the Pockels cell's behaviour, so as to know the input polarisation as a function of the voltage supplied to the Pockels cell.

Without the testing component in place and without the QWP, the Pockels cell fast axis was aligned at 45° to the linear polariser's axis, then the supplied voltage was varied between 0 to 5.5kV. The analyser was then rotated through 360°, measuring the intensity at regular angular intervals. The resulting plot is shown in Figure 8.
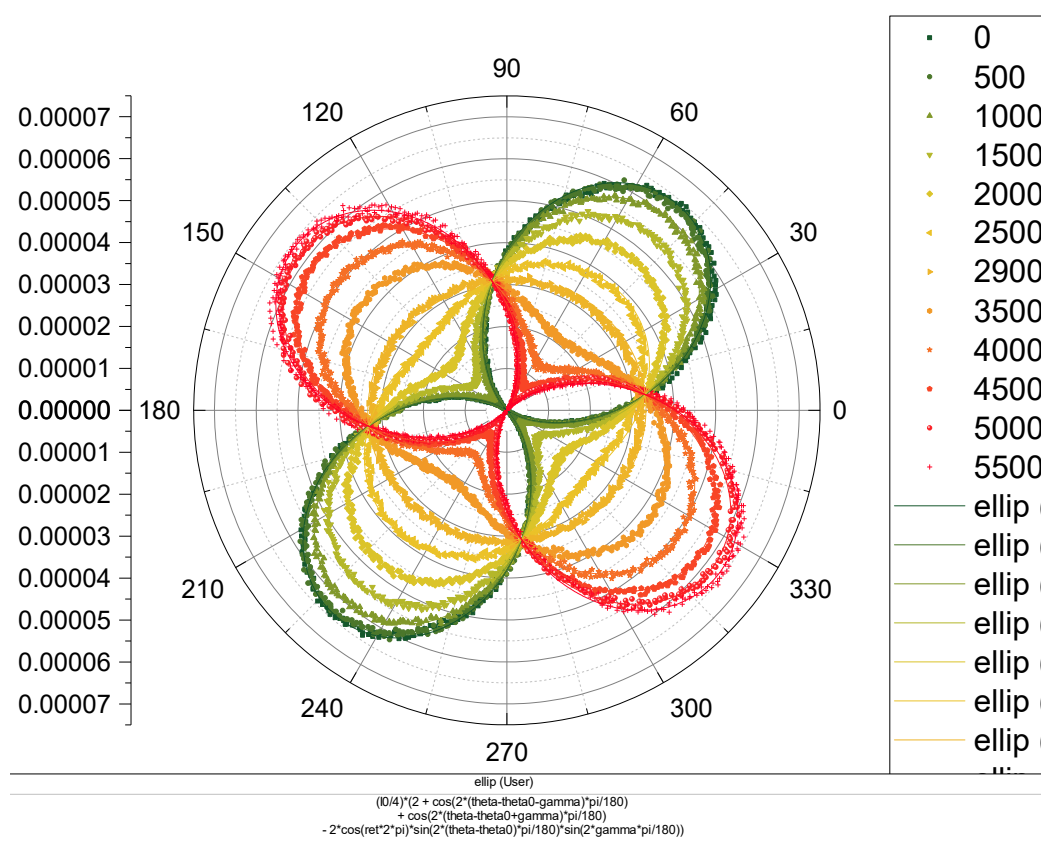

Figure 8 - Pockels cell calibration graph. Graphs are polar plots of measured intensity (AU) against analyser angle. The Pockels cell voltage is varied form 0 (dark green) to 5.5kV (red). The fitting function is seen at the bottom.

The polar plots are of measured intensity (AU) against analyser angle. At 0V, it can be seen that the output polarisation is linear; at about 2.9kV the polarisation becomes nearly circular (near the quarter-wave voltage), and at 5.5kV the polarisation is almost linear but rotated 90° (near the half-wave voltage). However, above 5.0kV, the high voltage power supply used turned out not to be stable, resulting in the data collected being more dispersed, as seen in the set of data for 5.5kV.

To extract the behaviour, I calculated a fitting function by modelling the optical system with Jones calculus, assuming the Pockels cell to behave as a waveplate of some retardance and some unknown fixed fast axis for each applied voltage. By setting retardance, amplitude and "fast axis" angle as fitting parameters, the fitted retardance was extracted and plotted against voltage in Figure 9.

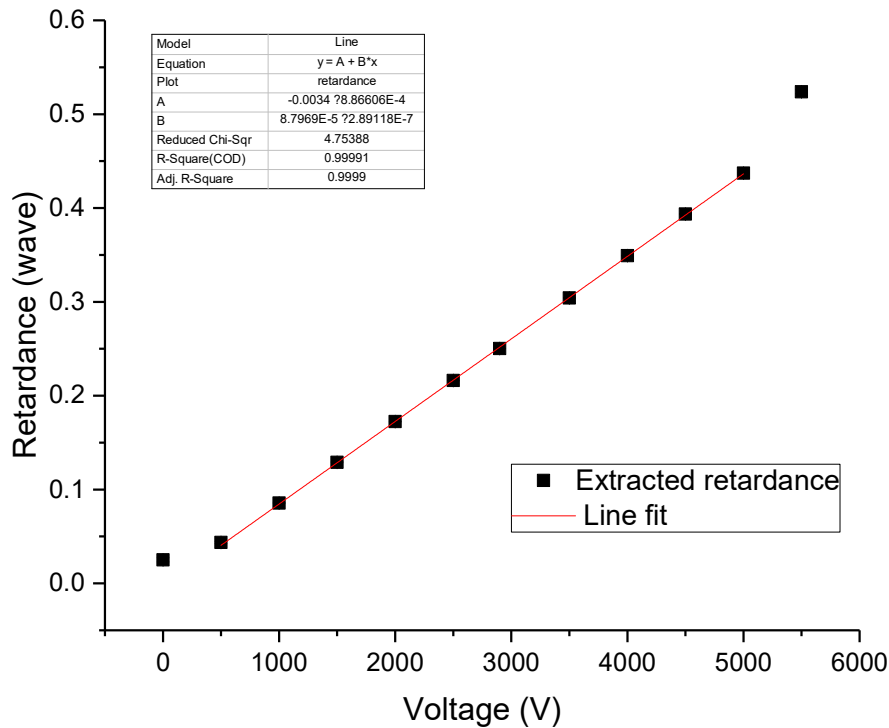| Model	Line
Equation	y = A + B*x
Plot	retardance
A	-0.0034 ?8.86606E-4
B	8.7969E-5 ?2.89118E-7
Reduced Chi-Sqr	4.75388
R-Square(COD)	0.99991
Adj. R-Square	0.9999

Figure 9 - Graph of extracted retardance of Pockels cell against applied voltage.

As Figure 9 shows, the Pockels cell retardance is indeed linear with applied voltage, if we disregard the points at 5.5kV (unstable power supply) and 0V (power supply giving nonzero voltage at lowest setting). The quarter-wave voltage can be calculated from the linear fit parameters to be (2.842 ± 0.009) kV.

3.5.3 Measurements of components

Once the Pockels cell was calibrated and ascertained to be functioning correctly, the behaviour of the polarisation of the various components was measured. The input polarisation would be measured first (without the component in place), then the various components would be put in place and the transmitted and reflected polarisations
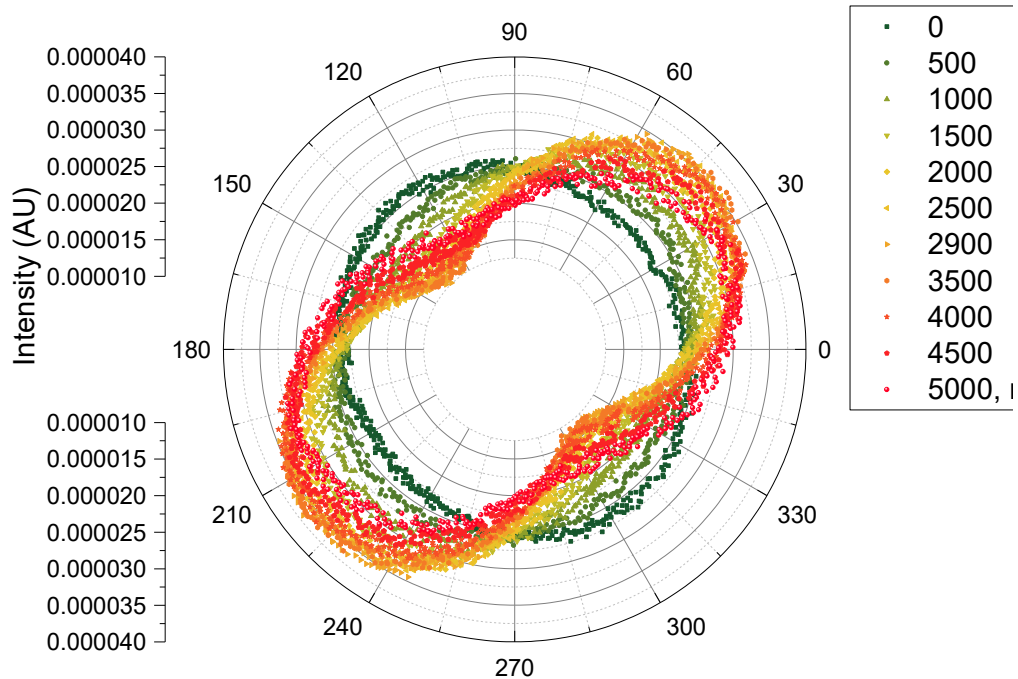
Figure 10 – Polarisation after reflection from VersaChrome Edge tunable shortpass filter, angled at 38° to the incident beam (same as in experiment setup). Initial polarisation before Pockels cell is linear at 45 degrees. An initially linear polarisation turns almost circular after reflection (dark green), an undesirable effect.

measured. Two components in particular were measured, the VersaChrome Edge tunable shortpass filter and the dielectric mirror used to combine the pump and probe beams. The results make it clear that the input polarisation is not preserved after reflection.

As seen in Figure 10, upon reflection by the tunable shortpass filter, initially linear polarisation is turned almost circular (dark green curve) even without a voltage across the Pockels cell. Changing the Pockels cell retardance also changes the polarisation, but not in a simple way. A fit was not performed because modelling the filter as a simple optical element with well-defined retardance did not yield any reasonable fits.

Figure 11 shows similar odd behaviour from the dichroic mirror, whereby initially linear polarisation (dark green curve) appears to remain mostly linear and rotated 45° at the quarter-wave voltage (yellow curve) instead of becoming circular.

After testing to make sure the reflected beams were not depolarised but indeed had well-defined polarisations, we finally realised that the polarisation changes in the reflected beams were probably due to the incident optical electric field being neither
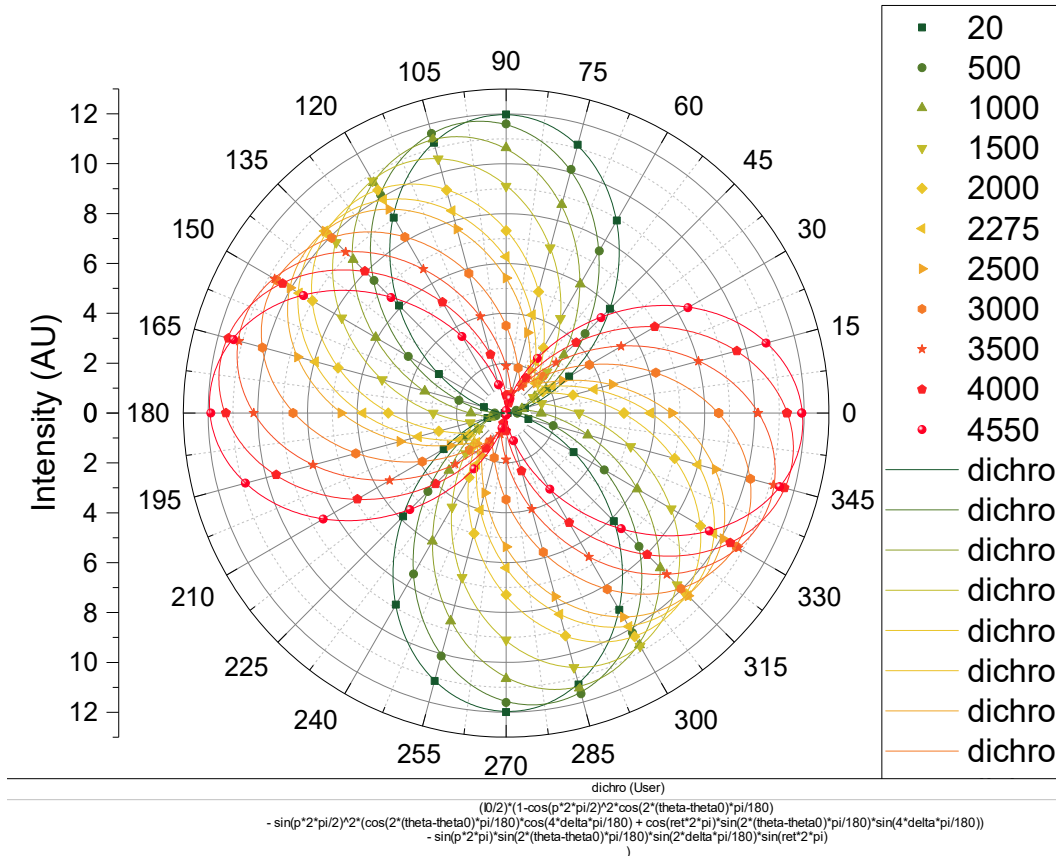
Figure 11 - Polarisation after reflection from dichroic mirror. Initial polarisation before Pockels cell is vertical linear. The reflected polarisation near the quarter-wave voltage (orange) is not circular as expected.

entirely in-plane nor entirely out-of-plane. The different electric field components would thus get transmitted or reflected differently as described by the Fresnel equations, and hence the output polarisation would in general not be the same as the input polarisation.

As the ultimate goal was to proceed with building the experimental setup, once we confirmed that the unexpected polarisation changes were due to the non-normal incidence and reflections of the signal beam on various components, we moved on to address the problem in the pump-probe setup rather than linger on an extended analysis of this problem.

In hindsight, it should have been obvious that the problem was the non-normal reflection off various optical components in the setup. This highlights the difficulty in polarisation spectroscopy setups in preserving the signal polarisation while trying to extract it.

3.5.4 Calibration of non-polarising beam splitter

As a solution to the polarisation problems, we decided upon using a non-polarising beam splitter (NPBS) to extract the second harmonic signal without altering it, despite losing half the signal intensity as a result. To ensure that this would indeed be the case,
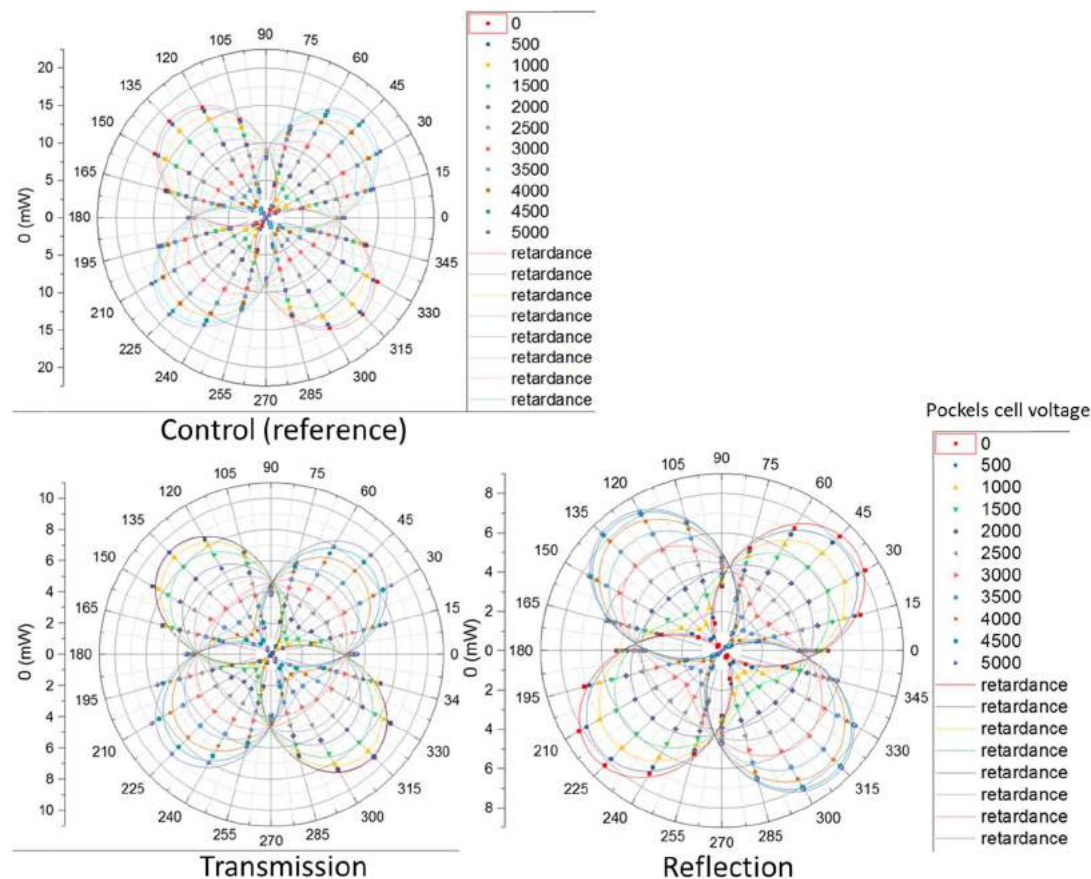

Figure 12 - Polarisation after transmission and reflection from NPBS. The reference input polarisation without NPBS present is also shown.

the same setup was used to check the transmitted and reflected beams from the NPBS before installing it in the main experiment. The data and fitted curves are shown in Figure 12.

Indeed, the signal polarisation appears to be preserved in both arms of the NPBS, barring the left-to-right flip caused by reflection. The fitting was accomplished by modelling the system (Pockels cell + NPBS) as a single waveplate of unknown retardance and fast axis angle, similar to the Pockels cell calibration described above. From the fitting, the retardance of the system with and without the NPBS was compared. As shown in Figure 13, the slope of the lines is close to 1, implying the NPBS does not affect the retardance of the system after transmission and reflection, and hence that it preserves the input beam's polarisation.
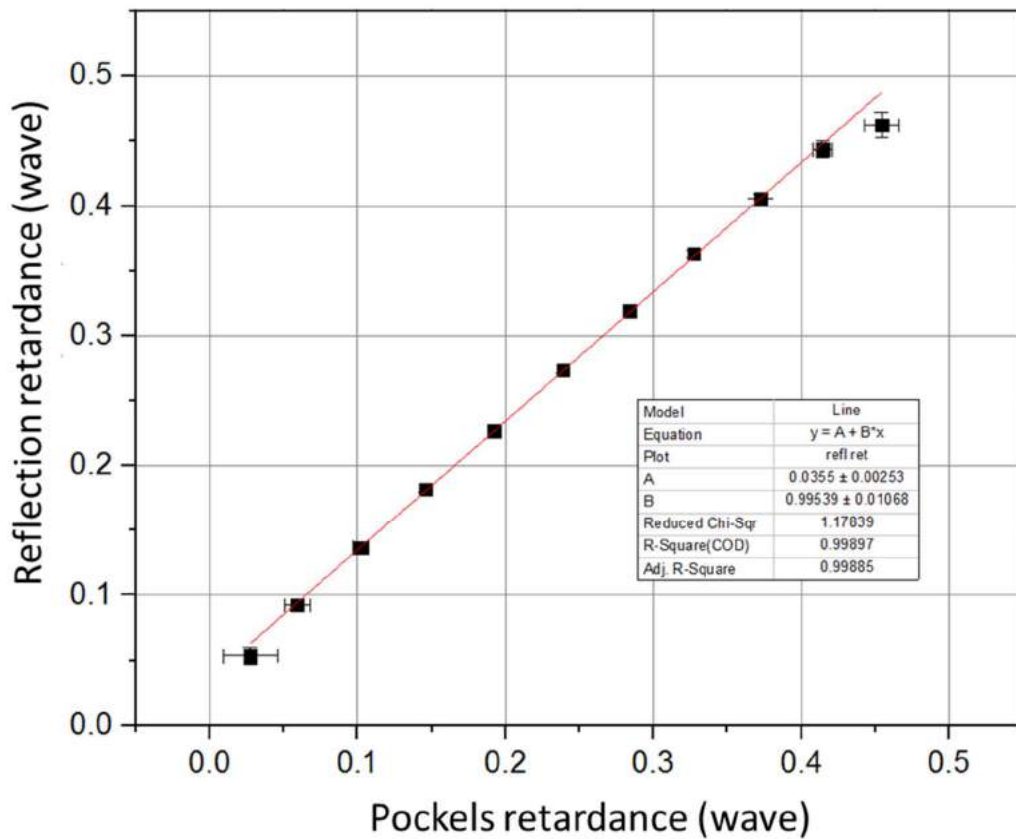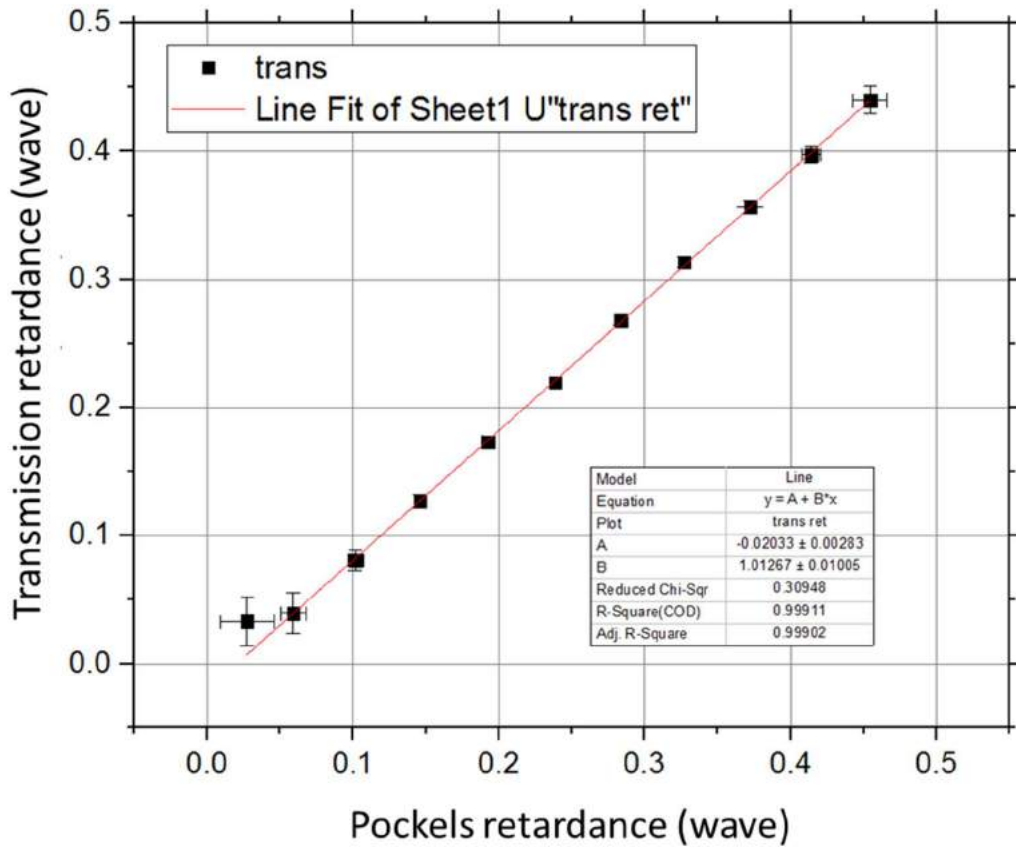
21

Figure 13 - Retardance of system with NPBS plotted against retardance of system without NPBS. Top: After transmission through NPBS. Bottom: After reflection from NPBS.

Chapter 4: **Modified experimental setup**

Having learnt from the polarisation issues, the detection part of the experimental setup had to be changed in order to avoid altering the signal we wanted to measure. The new version of the setup is shown in Figure 14.
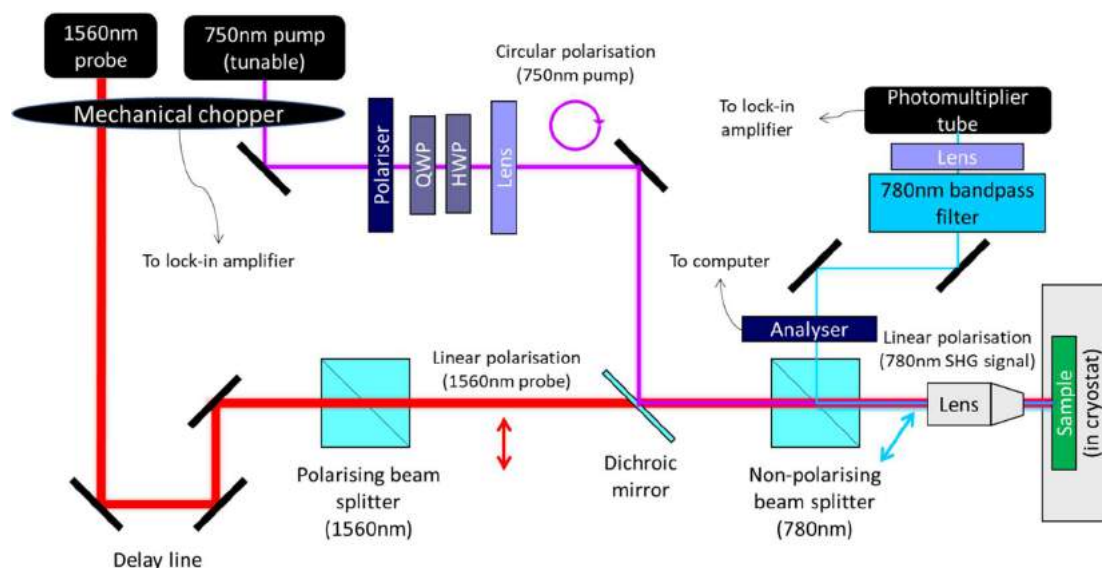

Figure 14 - Updated experimental setup to preserve signal polarisation. The mechanical chopper chops both beams at different frequency (see text).

The key changes made are with respect to the separation and collection of the signal. A non-polarising beam splitter is used to extract the 780nm second harmonic signal without affecting its polarisation (see section 3.5.4). It is then immediately passed through an analyser (rotating polariser) before being redirected to the PMT. Before the analyser, we want to keep the polarisation of the beam but after the analyser we only need to measure its intensity; hence it is of interest to analyse the signal as early in the optical system as possible. A 780nm bandpass filter is used just before the PMT to isolate the correct signal, and a lens is used to improve the coupling to the PMT.

The other change is the mechanical chopper; a dual-frequency chopper blade is used to chop both the pump and probe beams, enabling calibration and alignment to be done more easily with one (SHG from probe) or both (sum-frequency generation) beams. The chopper blade chops both beams, but by aligning the beams at radial positions with a different number of slots, they are chopped at different frequencies. By feeding the lock-in amplifier the one frequency or the other, or their sum or difference, signals of different frequency can be measured.

4.1.1 Aligning setup

Once the setup was successfully modified, the next step was to ensure the beams were correctly overlapped on the sample.

The spatial overlapping was achieved by adjusting the mirrors and lenses while using a CCD camera to observe the beam spots. This allows us to adjust the pump beam waist position to match that of the probe beam both longitudinally (lens) and transversally (mirrors).

The temporal overlapping is achieved by varying the delay line position. In order to check for this overlap, we use SFG from both beams as a diagnostic. SFG is a good way to check for temporal overlap, as it will only be present if pulses from both beams arrive well overlapped at the sample in time and space.

By adjusting the sample position, we first maximise SHG from the probe beam, we ensure that the sample is located at the spatial beam waist of the probe beam, which is also the waist of the pump beam.

Then, by changing the reference frequency to the lock-in amplifier and replacing the 780nm bandpass filter with a 640nm shortpass filter, we can measure the SFG (wavelength 506nm). This involves adjusting the position of the delay line and scanning across its range until the pulses arrive synchronously at the sample, yielding a maximum SFG signal.

I improved some existing code and wrote some new code to automate the data collection procedures for the second harmonic polarisation analysis and the delay line scanning, and performed these scans on the samples to try and confirm that the system was indeed well-aligned.

4.1.2 SHG and SFG from bulk LNB

The initial alignment and debugging was done using bulk LNB, which has a strong second-order susceptibility. The procedure was carried out in the manner described above. Figure 16 shows the SHG signal from bulk LNB measured as a function of analyser angle and fitted, confirming that the probe beam is well-aligned; Figure 15 shows the SFG signal from a delay line scan, displaying a peak in the signal near the

24

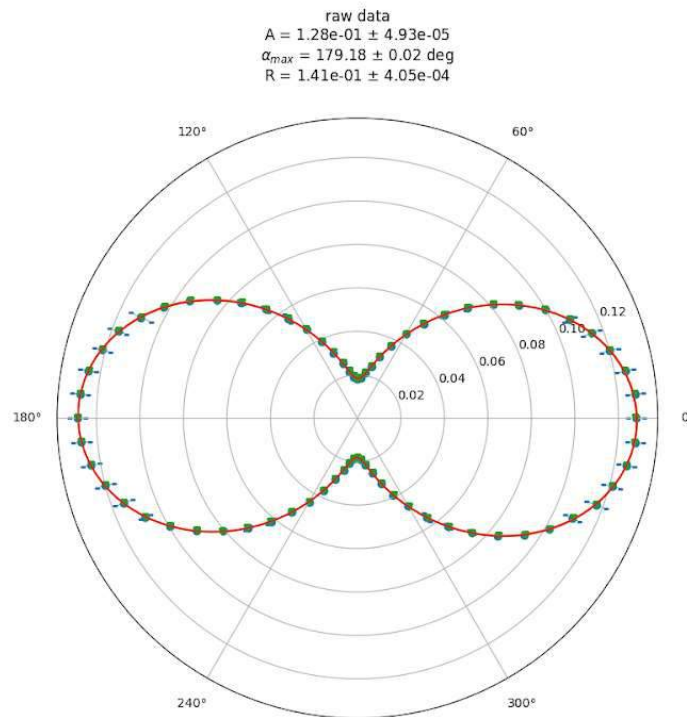delay line position of 5.955mm. This indicates that there is temporal overlap of the pulses at the sample.

Figure 16 - Second harmonic generation from bulk LiNbO$_3$ from linearly polarised probe beam. Intensity (AU) as a function of analyser angle, showing the shape of linearly polarised light. Blue points are data, red and orange lines are fits.
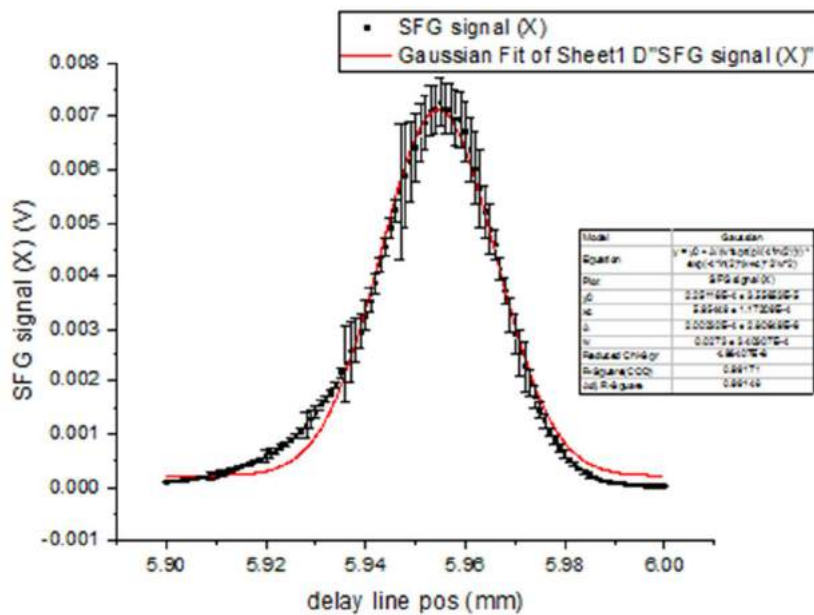
Figure 15 - Sum frequency signal from bulk LiNbO3 as a function of delay line position. There is a clear peak close to 5.955mm, where the pulses arrive at the sample at the same time.

25

4.1.3 Confirmation of SHG and SFG with TMD samples

As the beam overlap is a property of the geometry of the beams and the setup alone, it should not depend on which type of sample is used. But when using monolayer WSe_2 (the desired sample for the actual valley polarisation experiment), SHG was obtained (Figure 17; t

Figure 17 - Second harmonic generation from 2H-phase WSe_2. Intensity (AU) as a function of analyser angle, showing the shape of linearly polarised light. Blue points are data, red and orange lines are fits.
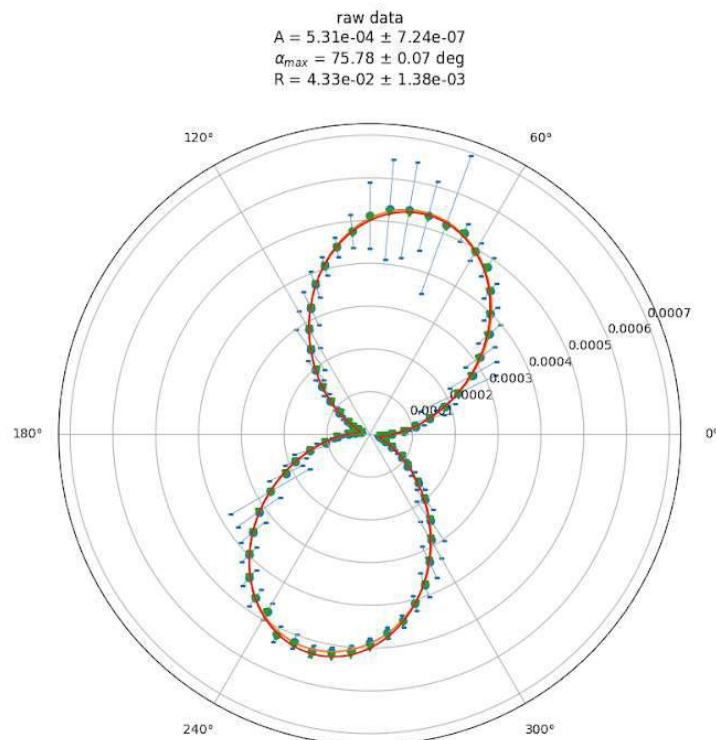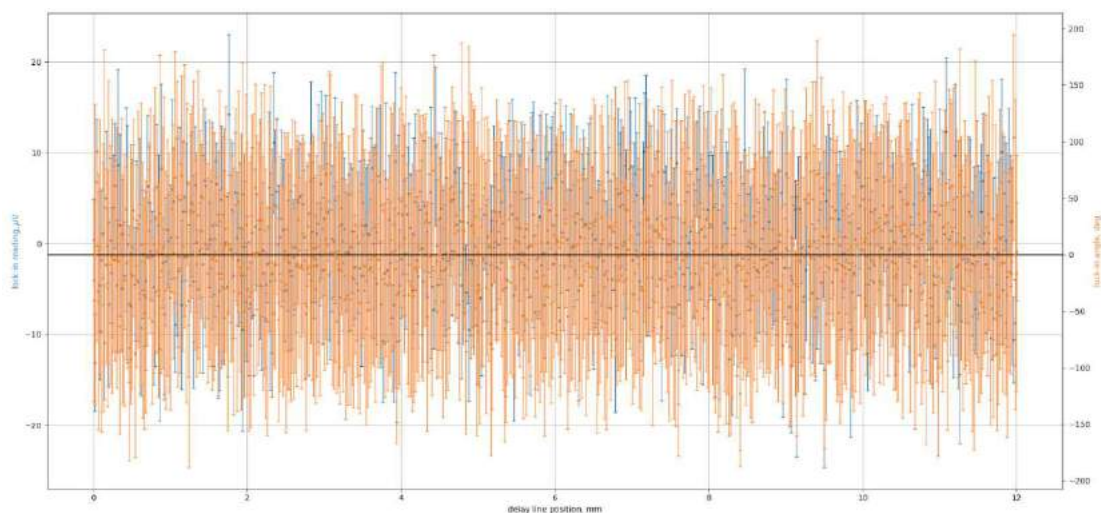

Figure 18 - Delay line scan of 3R-phase MoS2. Blue points and error bars are the lock-in X (signal) reading, orange points and error bars are the lock-in phase. The phase is not consistent anywhere in the delay line range, indicating that any signal is hidden by noise.

he polarisation orientation depends on the orientation of the sample, so will not generally be aligned to the horizontal axis) but not SFG until recently.

It is known that 3R-phase TMDs do not exhibit inversion symmetry in even-layer stacks, and so will continue to have a strong second-order response from multilayer stacks. Nevertheless, we encountered the same problem for 3R-phase MoS_2, where we obtained SHG but not SFG. Figure 18 shows a delay line scan across the whole range where no SFG signal was obtained.

Eventually, we concluded that the problem was not that the SFG signal had vanished, but simply that it was so small that the signal-to-noise ratio made it effectively undetectable. There are several reasons for this.

The bulk LNB consists of many more layers than the few-layer TMD samples, so more layers contribute to the SHG and SFG signals (up to a certain surface depth) and thus the signal from bulk LNB is stronger.

The power of the supercontinuum pump is also weak, as firstly it is a supercontinuum laser, and also its power was deliberately reduced to avoid saturating and/or burning the TMD samples. When measured just before the sample with a powermeter, the pump power was about 2 μW, as compared to the 1560nm probe which was around 6 mW.

As proof of this guess and also proof that the setup was correctly built, by amplifying the PMT signal, turning its gain up to the maximum, removing the analyser and increasing the integration time of the lock-in amplifier to 0.3s, we managed to obtain a faint SFG signal from the 3R-MoS$_2$ sample (Figure 19).
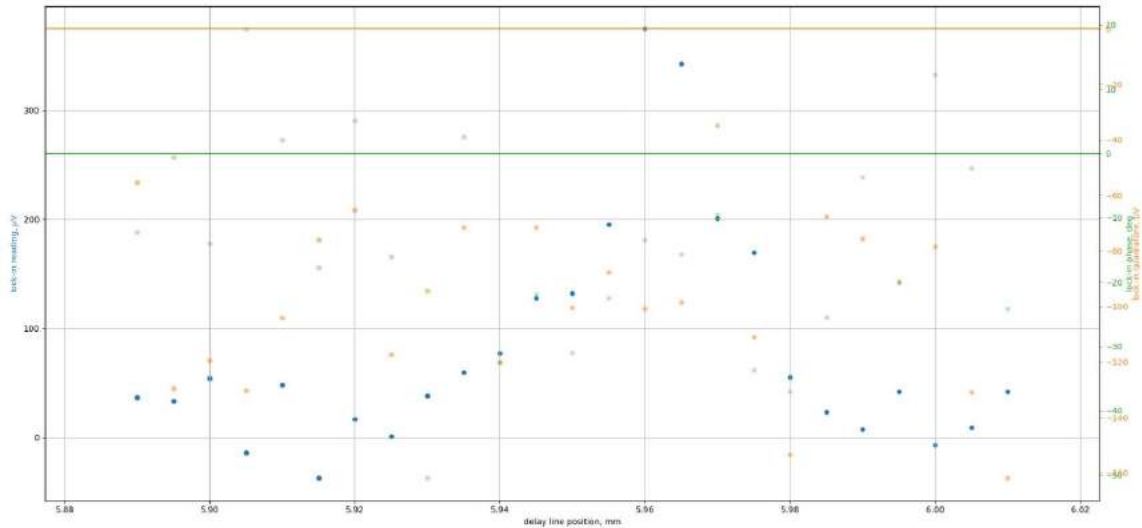

Figure 19 - Sum frequency signal from MoS$_2$ with maximum signal amplification. The blue points represent the lock-in signal (X), the orange points the lock-in quadrature (Y), and green points the lock-in phase. A peak in the signal is observed near 5.96mm. Error bars have been suppressed for clarity.

The peak in the signal occurs at a delay line position of near 5.96mm, consistent with the results from testing with LNB. However, despite this effort, the signal-to-noise ratio is still small (estimating from Figure 19, about 5:1), and the lock-in phase is still not constant over this range.

4.1.4 Impact on experiment and current status

While the sum-frequency generation is only a check on the setup and not a critical quantity measured in the actual experiment, we still would like it to be easy to check the alignment of the setup with it. In principle, we have already confirmed that the setup is good and can potentially be used for experiments.

The current state of the experiment is that we will attempt to use a Kymera 328i spectrograph from Andor to analyse the signals instead of the PMT. The main advantage of using a spectrograph instead is that the entire spectrum of the signal can be seen. This is in contrast with the lock-in amplifier where just a single number

representing the intensity of the signal can be retrieved at a time, and where the precise wavelength of the signal is not known and has to be inferred from the filters in the experimental setup and the settings used on the lock-in amplifier and chopper.

With the spectrograph, the different signals (SHG, SFG) could be seen and compared at the same time for instance, ensuring that the pulses are well overlapped during a run.

Once the spectrograph is integrated into the setup, if we choose to use it, we should be ready to measure actual data using the WSe_2 sample.

Chapter 5: **Conclusion**

5.1 Further works

There remains some further work to be done on this setup before data can be acquired. I will continue to work on this for my MSc thesis (which is concurrently ongoing). Notably, the spectrometer will have to be integrated with the existing setup and with the Python codebase we are using to collect data, and the cryostat eventually brought into operation.

The main move forward is to collect experimental data with this setup and analyse it. With experimental data at hand, it will be possible to evaluate the viability of SHG spectroscopy as a means to measure valley polarisation.

In addition, further improvements or avenues of exploration could be done with the setup, including partially rebuilding the setup to allow the sample to be mounted horizontally instead of vertically, or to use a different detection system like a balanced photodiode to reduce noise from the laser.

If SHG spectroscopy proves useful in probing valley polarisation in TMDs, there is a possibility that the method could be applied to other materials, including graphene.

Bibliography

[1] Z. Ye, D. Sun, and T. F. Heinz, 'Optical manipulation of valley pseudospin', *Nature Physics*, vol. 13, no. 1, pp. 26–29, Sep. 2016.

[2] F. Hipolito and V. M. Pereira, 'Second harmonic spectroscopy to optically detect valley polarization in 2D materials', *2D Materials*, vol. 4, no. 2, p. 021027, May 2017.

[3] Y. W. Ho *et al.*, 'Measuring valley polarization in transition metal dichalcogenides with second-harmonic spectroscopy', *arXiv:1903.01367 [cond-mat, physics:physics]*, Mar. 2019.

[4] D. Xiao, W. Yao, and Q. Niu, 'Valley-Contrasting Physics in Graphene: Magnetic Moment and Topological Transport', *Physical Review Letters*, vol. 99, no. 23, Dec. 2007.

[5] L. E. Golub and S. A. Tarasenko, 'Valley polarization induced second harmonic generation in graphene', *Physical Review B*, vol. 90, no. 20, Nov. 2014.

[6] D. Xiao, G.-B. Liu, W. Feng, X. Xu, and W. Yao, 'Coupled Spin and Valley Physics in Monolayers of MoS2 and Other Group-VI Dichalcogenides', *Physical Review Letters*, vol. 108, no. 19, May 2012.

[7] K. F. Mak, D. Xiao, and J. Shan, 'Light–valley interactions in 2D semiconductors', *Nature Photonics*, vol. 12, no. 8, pp. 451–460, Aug. 2018.

[8] K. F. Mak, K. He, J. Shan, and T. F. Heinz, 'Control of valley polarization in monolayer MoS2 by optical helicity', *Nature Nanotechnology*, vol. 7, no. 8, pp. 494–498, Aug. 2012.

[9] D. Vanderbilt, *Berry phases in electronic structure theory*. Cambridge: Cambridge University Press, 2018.

[10] D. Xiao, M.-C. Chang, and Q. Niu, 'Berry phase effects on electronic properties', *Reviews of Modern Physics*, vol. 82, no. 3, pp. 1959–2007, Jul. 2010.

[11] K. F. Mak, K. L. McGill, J. Park, and P. L. McEuen, 'The valley Hall effect in MoS2 transistors', *Science*, vol. 344, no. 6191, pp. 1489–1492, Jun. 2014.

[12] T. LaMountain, H. Bergeron, I. Balla, T. K. Stanev, M. C. Hersam, and N. P. Stern, 'Valley-selective optical Stark effect probed by Kerr rotation', *Physical Review B*, vol. 97, no. 4, Jan. 2018.

[13] C. R. Zhu *et al.*, 'Exciton valley dynamics probed by Kerr rotation in WSe 2 monolayers', *Physical Review B*, vol. 90, no. 16, Oct. 2014.

[14] H. Zeng, J. Dai, W. Yao, D. Xiao, and X. Cui, 'Valley polarization in MoS2 monolayers by optical pumping', *Nature Nanotechnology*, vol. 7, no. 8, pp. 490–493, Aug. 2012.

[15] T. O. Wehling, A. Huber, A. I. Lichtenstein, and M. I. Katsnelson, 'Probing of valley polarization in graphene via optical second-harmonic generation', *Physical Review B*, vol. 91, no. 4, Jan. 2015.

[16] R. W. Boyd, *Nonlinear optics*, 3rd ed. Amsterdam ; Boston: Academic Press, 2008.

[17] D. Lagarde *et al.*, 'Carrier and Polarization Dynamics in Monolayer MoS 2', *Physical Review Letters*, vol. 112, no. 4, Jan. 2014.

[18] H. G. Rosa *et al.*, 'Characterization of the second- and third-harmonic optical susceptibilities of atomically thin tungsten diselenide', *Scientific Reports*, vol. 8, no. 1, Dec. 2018.

[19] K. He *et al.*, 'Tightly Bound Excitons in Monolayer WSe 2', *Physical Review Letters*, vol. 113, no. 2, Jul. 2014.

[20] K. F. Mak, C. Lee, J. Hone, J. Shan, and T. F. Heinz, 'Atomically Thin MoS 2 : A New Direct-Gap Semiconductor', *Physical Review Letters*, vol. 105, no. 13, Sep. 2010.

[21] A. V. Kolobov and J. Tominaga, *Two-dimensional transition-metal dichalcogenides*. Cham: Springer, 2016.

[22] J. R. Schaibley *et al.*, 'Valleytronics in 2D materials', *Nature Reviews Materials*, vol. 1, no. 11, Nov. 2016.

[23] X. Xu, W. Yao, D. Xiao, and T. F. Heinz, 'Spin and pseudospins in layered transition metal dichalcogenides', *Nature Physics*, vol. 10, no. 5, pp. 343–350, May 2014.

[24] L. M. Malard, T. V. Alencar, A. P. M. Barboza, K. F. Mak, and A. M. de Paula, 'Observation of intense second harmonic generation from MoS2 atomic crystals', *Physical Review B*, vol. 87, no. 20, May 2013.

[25] R. I. Woodward *et al.*, 'Characterization of the second- and third-order nonlinear optical susceptibilities of monolayer MoS 2 using multiphoton microscopy', *2D Materials*, vol. 4, no. 1, p. 011006, Nov. 2016.

[26] A. Autere, H. Jussila, Y. Dai, Y. Wang, H. Lipsanen, and Z. Sun, 'Nonlinear Optics with 2D Layered Materials', *Advanced Materials*, vol. 30, no. 24, p. 1705963, Jun. 2018.

[27] G. Wang *et al.*, 'Giant Enhancement of the Optical Second-Harmonic Emission of WSe 2 Monolayers by Laser Excitation at Exciton Resonances', *Physical Review Letters*, vol. 114, no. 9, Mar. 2015.

[28] K. Hao *et al.*, 'Direct measurement of exciton valley coherence in monolayer WSe2', *Nature Physics*, vol. 12, no. 7, pp. 677–682, Jul. 2016.

[29] A. M. Jones *et al.*, 'Optical generation of excitonic valley coherence in monolayer WSe2', *Nature Nanotechnology*, vol. 8, no. 9, pp. 634–638, Sep. 2013.